ACS ENVIRONMENTAL Au
AN OPEN ACCESS JOURNAL OF THE AMERICAN CHEMICAL SOCIETY

pubs.acs.org/environau
Article

Coconut Shell Waste-Derived Porous Carbon-Supported Sn Catalysts for Efficient Electrochemical CO_2 Reduction to Formic Acid and Deuterated Formic Acid

Chen Qin, Gevindu Masakorala, Muhammed Mohideen, Thisus Samarasekara, Long Zhang, Wenlei Zhu,* Yang Zhou,* and Charitha Thambiliyagodage*

Cite This: ACS Environ. Au 2026, 6, 144−153
Read Online

ACCESS | Metrics & More | Article Recommendations | Supporting Information

ABSTRACT: Industrial-level electrochemical CO_2 reduction reaction (CO_2RR) to form $HCOO^-$ and $DCOO^-$ requires robust Sn catalysts with high performance. In this study, the hydrothermal method was employed to load varying amounts of Sn precursors onto waste biomass-derived porous carbon to investigate the structure−activity relationship between Sn loading forms and $HCOO^-$ selectivity. Through comprehensive *ex/in situ* characterizations, we discovered that with 5% Sn precursor addition, highly dispersed SnO_2 nanoparticles formed on the carbon support, enabling the catalyst to exhibit exceptional $HCOO^-$ activity (Faradaic efficiency exceeding 90%) across a broad potential window. *In situ* attenuated total reflection Fourier transform infrared spectroscopy (ATR-FTIR) and *in situ* Raman spectroscopy revealed that the highly dispersed SnO_2 nanoparticles enhance the stability of the *OCHO intermediate. Furthermore, when H_2O was replaced with D_2O, the generation of $DCOO^-$ was observed, and good selectivity was maintained. This study provides a facile strategy for waste biomass conversion and the design of Sn-based catalysts for $DCOO^-$ production.

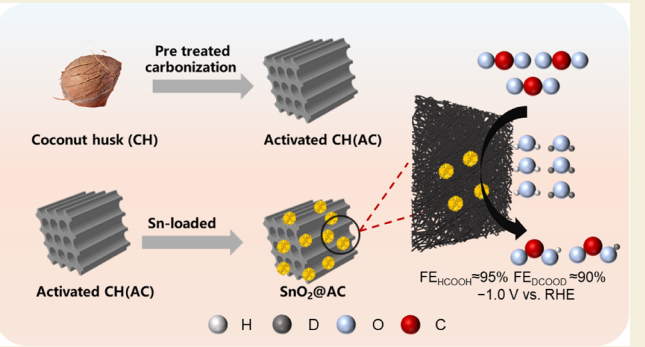

KEYWORDS: *biomass-derived porous carbon, Sn-based catalysts, CO_2 reduction, deuterated formic acid, catalytic mechanism*

INTRODUCTION

The increasing atmospheric CO_2 concentration resulting from fossil fuel consumption has resulted global climate crisis.[1−6] The development of carbon-neutral technologies is a practical strategy to mitigate the issue.[7−10] Electrochemical CO_2 reduction (CO_2RR) is an excellent route to producing value-added chemicals from CO_2.[11−14] Among various reduction products, $HCOO^-$ holds significant appeal as a liquid hydrogen carrier and essential chemical feedstock. However, the widespread implementation of CO_2RR hinges critically on the availability of efficient, stable, and cost-effective electrocatalysts.[15−17] While noble metals (e.g., Pd, Pt) exhibit high performance for $HCOO^-$ generation, their scarcity and exorbitant cost impede large-scale application.[18−20] Furthermore, its isotopically labeled derivative, deuterated formate ($DCOO^-$), is a promising product due to its applications in drug development and nuclear magnetic resonance (NMR) analysis, and enhancing the lifespan of organic light-emitting diode devices. Nevertheless, conventional synthesis methods face challenges such as complex procedures and harsh conditions.[21] Replacing H_2O with D_2O to produce $DCOO^-$ via CO_2RR offers a more straightforward and efficient approach.

Sn-based catalysts have garnered significant research interest due to their low toxicity and ready availability.[22−24] Especially, tin dioxide (SnO_2)-based catalysts represent a highly promising solution due to their unique ability to stabilize the *OCHO intermediate key precursor for $HCOO^-$ formation via the proton-coupled electron transfer pathway.[25−27] Experimental evidence clarifies that Sn^{2+}, not Sn^{4+}, is the active site for CO_2-to-$HCOO^-$ conversion, as Sn^{2+} facilitates key carbonate intermediate formation.[28,29] Furthermore, SnO_2 suffers from agglomeration and reduction to metallic Sn^0 under reaction conditions, leading to catalyst deactivation and compromised performance.[28−30] These challenges underscore the urgent need to achieve dispersion of active sites and stabilization of the Sn oxidation state during CO_2RR through compositing with advanced conductive supports.

Received: September 15, 2025
Revised: October 26, 2025
Accepted: October 29, 2025
Published: November 5, 2025

Porous carbon materials, especially those derived from waste biomass (e.g., coconut shells), are ideal supports due to their high surface area,[31,32] excellent conductivity, and chemical stability.[33] More importantly, this approach transforms abundant waste into high-value materials, aligning with circular economy principles.[34,35] The inherent hierarchical porosity of biomass can be tailored to create an ideal environment for immobilizing and dispersing Sn-based catalysts.[36,37] Waste coconut shells possess a unique inherent hierarchical porosity.[38,39] Through controlled pyrolysis and activation processes, they can be converted into carbon supports with highly developed pore networks, providing an ideal support environment for the immobilization of Sn-based catalysts and dispersion of active sites.[40−42] Therefore, we aim to utilize the ideal support derived from waste coconut shells to modulate the dispersion of SnO_2, thereby developing a more efficient Sn-based catalyst for CO_2RR.[43,44]

Here, we report the rational design and synthesis of a high-performance electrocatalyst for the efficient CO_2RR to $HCOO^-/DCOO^-$. The catalyst is fabricated by strategically loading SnO_2 species onto porous carbon derived from waste coconut shells. Crucially, the activated porous carbon (AC), as an engineered multifunctional support, effectively inhibits the agglomeration of SnO_2 until a Sn doping level of 10% is reached, at which point diffraction peaks attributed to SnO_2 are detectable by XRD. Characterization of the valence state of Sn on the catalyst surface via quasi *in-situ* XPS also reveals that after loading onto the AC, the reduction of Sn^{4+} is arrested at Sn^{2+}, which acts as an active site to promote the formation of $HCOO^-/DCOO^-$. Moreover, when the doping level is 5%, the proportion of monodispersed Sn^{2+} is the highest, and the number of active sites is the greatest, resulting in superior $HCOO^-/DCOO^-$ performance. This conclusion is further supported by in situ Raman and infrared spectroscopy. The spectra show that the Sn-5% catalyst exhibits excellent adsorption capacity for the *OCHO intermediate. This intermediate is key to achieving the high selectivity for $HCOO^-$. Within the potential range of −0.9 V to −1.1 V (vs RHE), the selectivity for $HCOO^-$ remains above 95%, while that for $DCOO^-$ is all above 60%. (Unless otherwise specified, all potentials are against the RHE.)

This work systematically elucidates how SnO_2 is efficiently loaded and dispersed on the porous carbon framework. It establishes a structure−activity relationship between the tin valence state in the SnO_2/porous carbon composite and product selectivity. The study also reveals the critical role of the porous carbon support in dispersing active sites and stabilizing the tin valence state. Based on these findings, we propose a novel strategy for highly efficient $DCOO^-$ generation by regulating Sn^{2+} active sites in combination with a D_2O electrolyte. This work demonstrates the successful conversion of waste biomass into a high-value functional material. Moreover, it presents, for the first time, a systematic investigation into the structure−activity relationship between Sn valence states and the selectivity of $HCOO^-/DCOO^-$. Ultimately, this research successfully achieves the efficient production of $DCOO^-$ via the CO_2RR.

EXPERIMENTAL METHODS

Materials

Coconut husk was collected from the Kuliyapitiya area, Sri Lanka. Tin(II) chloride ($SnCl_2·2H_2O$, AR), Potassium bicarbonate ($KHCO_3$, AR), and Trisodium citrate dihydrate ($Na_3C_6H_5O·2H_2O$, AR) were purchased from Sinopharm Chemical Reagent Co., Ltd. (Shanghai, China). Hydrochloric acid (HCl, AR), nitric acid (HNO_3, AR), sodium hydroxide (NaOH, AR), and Nafion (5 wt %) were purchased from Macklin. Dimethyl sulfoxide and deuterium water were purchased from Rhawn. All chemicals were used as received without further purification.

Catalysts Preparation of Sn-5%

100 mg of the treated AC was dispersed in 25 mL of ultrapure water. The specific treatment procedure for AC has been described in detail in the Supporting Information. Subsequently, 14.970 mg of $SnCl_2·2H_2O$ and 48.74 mg of $Na_3C_6H_5O_7·2H_2O$ were added to the aqueous solution under vigorous stirring. Following this, 1 mL of 0.2 M NaOH was added dropwise to the above mixture with continuous stirring for 30 min. Then the obtained white precipitate was stirred and washed until a neutral pH was reached. The mixture solution was transferred to a stainless-steel hydrothermal autoclave with a Teflon liner and followed by heating at 180 °C for 12 h. Finally, the prepared samples were collected by centrifugal washing with deionized water three times and dried at 65 °C for 6 h in a vacuum oven. The detailed synthesis procedures for the remaining catalysts, as well as for the SnO_2 powder, are provided in the Supporting Information.

Catalysts Characterization

Scanning electron microscope (SEM) images were obtained on a JSM-7800F (JEOL, Japan). X-ray diffraction (XRD) data were recorded using a Shimadzu XRD-6000 diffractometer, with Cu Kα radiation (Shimadzu, Japan). Transmission electron microscopy (TEM) characterization was conducted using a JEM-2800 electron microscope (JEOL, Japan) operated at 200 kV. X-ray photoelectron spectroscopy (XPS) was performed using a PHI 5000 VersaProbe (Ulvac-Phi, Japan) with an Al Kα (1486.6 eV) excitation source. *In situ* Raman spectra were collected on a Horiba LabRAM HR Evolution spectroscopy at the excitation wavelength of 633 nm using a catalyst-coated gas diffusion layer as the working electrode. FTIR spectra were obtained using a Thermo Scientific NICOLET iS50.

Electrochemical Measurements

All electrochemical measurements were conducted on an electrochemical workstation (Gamry Interface 1000E). To prepare the cathode electrode, a mixture that contains 5 mg of catalysts, 2 mL of isopropanol, and 50 μL of Nafion ionomer solution (5 wt % in isopropanol) was first sonicated for 60 min to obtain a catalyst ink. Then, 2 mL of the catalyst ink was sprayed onto a gas diffusion layer to achieve a catalyst loading of ∼0.8 mg cm^{-2}. Electrochemical tests were conducted in an electrochemical flow cell, which includes a gas chamber, a cathodic chamber, and an anodic chamber. A 0.5 M $KHCO_3$ solution was used as the anolyte and catholyte. A proton exchange membrane (Nafion N115) was used to separate the anodic and cathodic chambers. A piece of titanium mesh loaded with iridium dioxide was used as the counter electrode, and a saturated Ag/AgCl was used as the reference electrode. The high-purity CO_2 (99.999%, 20 cc) was introduced on the back side of the gas diffusion layer, and the electrolyte flowed in both cathodic and anodic chambers with a flow rate of 2 mL min^{-1}. The electrochemically active surface area (ECSA) was

https://doi.org/10.1021/acsenvironau.5c00213
ACS Environ. Au 2026, 6, 144−153

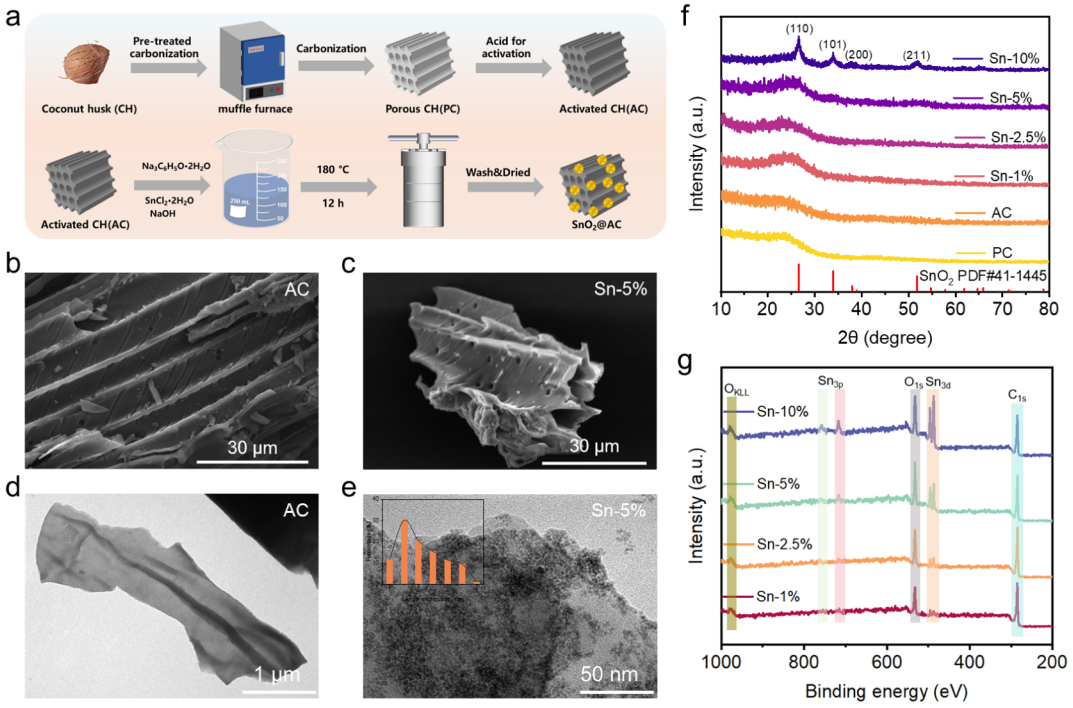

Figure 1. (a) Schematic diagram of the Sn-catalyst synthesis process. SEM images of AC (b) and Sn-5% (c). TEM images of AC (d) and Sn-5% (e). (f) XRD patterns of the catalysts. (g) XPS survey spectrum of Sn-loaded catalysts.

determined by measuring double-layer capacitance (C_{dl}). C_{dl} was determined by measuring the capacitive current associated with double-layer charging from the scan-rate dependence of the cyclic voltammogram (CV). All potentials were converted to the reversible hydrogen electrode by E (RHE) = E (Ag/AgCl) + 0.197 V + 0.0591 V × pH without iR compensation.

Product Analysis

The gaseous products were monitored by an online gas chromatograph (GC, GC9790PLUS) equipped with a thermal conductivity detector (TCD) and a flame ionization detector (FID). The liquid products in cathode chambers were collected after electrolysis and analyzed by ^{1}H nuclear magnetic resonance (NMR, Bruker AV400) using DMSO as the internal standard and D_2O as a proton signal source.

The Faraday efficiency (FE) of gas products was calculated by the following equation:

$$FE\% = \frac{I}{I_{total}} = \frac{zFnV}{I_{total}} \times 100\%$$

Where I is the partial current density of a specific product. I_{total} is the total current density collected in the bulk electrolysis at an applied potential. z is the number of electrons involved in the formation of a specific product. F is the Faraday constant, 96485 C mol^{-1}. n is the mole fraction of the product. V is the gas volumetric flow rate of gas.

The FE of the liquid products was calculated as

$$FE = z \cdot F \cdot \frac{n}{Q}$$

Where z is the number of electrons transferred per mole of gas product, F is the Faraday constant (96500 C mol^{-1}), n is the total amount of the liquid products determined from NMR (mole), and Q is the total amount of charge passed through the cathode (A·s).

RESULTS AND DISCUSSION

Synthesis and Characterization of Catalysts

To investigate the structure−activity relationship between the loading form of Sn on AC and the selectivity of $HCOO^-$, we conducted a series of characterizations on the synthesized catalysts. The synthesis schematic of the catalyst is shown in Figure 1a. After the acid-washing activation treatment of the porous carbon, varying amounts of Sn were loaded via the hydrothermal method. SEM images of the materials were collected to study the surface morphology. SEM images taken in the longitudinal sections of the materials are shown in Figure 1b−c. The SEM images taken of the cross sections are shown in Figures S1−S6. As the SEM images of the cross-sectional area show, circular to irregular-shaped macropores are present in a network. The SEM images of the longitudinal area show tubes or channels, where the macropores observed are the openings of such pathways. It is clear that upon deposition of SnO_2 nanomaterials, the macropore network has not been disrupted. Furthermore, Sn-10% was analyzed using Energy Dispersive X-ray Spectrometry (EDS) to study the elemental distribution on the sample. The SEM image of Sn-10% selected for the EDS analysis is shown in Figure S7a. Energy Dispersive X-ray Spectrometry (EDS) analysis of Sn-10% confirmed the presence of Sn (3.3 wt %), along with C (72.2 wt %) and O (22.6 wt %), on the catalyst surface (Figure S7). Elemental mapping revealed that Sn was successfully incorporated but nonuniformly distributed across the carbon matrix, consistent with the intended loading amount (10 wt %). In contrast, C and O were homogeneously abundant, the latter attributed to the oxygen-rich functional groups introduced during HNO_3 activation of the coconut husk-derived carbon. A small amount of Si (1.9 wt %), inherent to the biomass precursor, was also detected with an uneven distribution.

https://doi.org/10.1021/acsenvironau.5c00213
ACS Environ. Au 2026, 6, 144−153

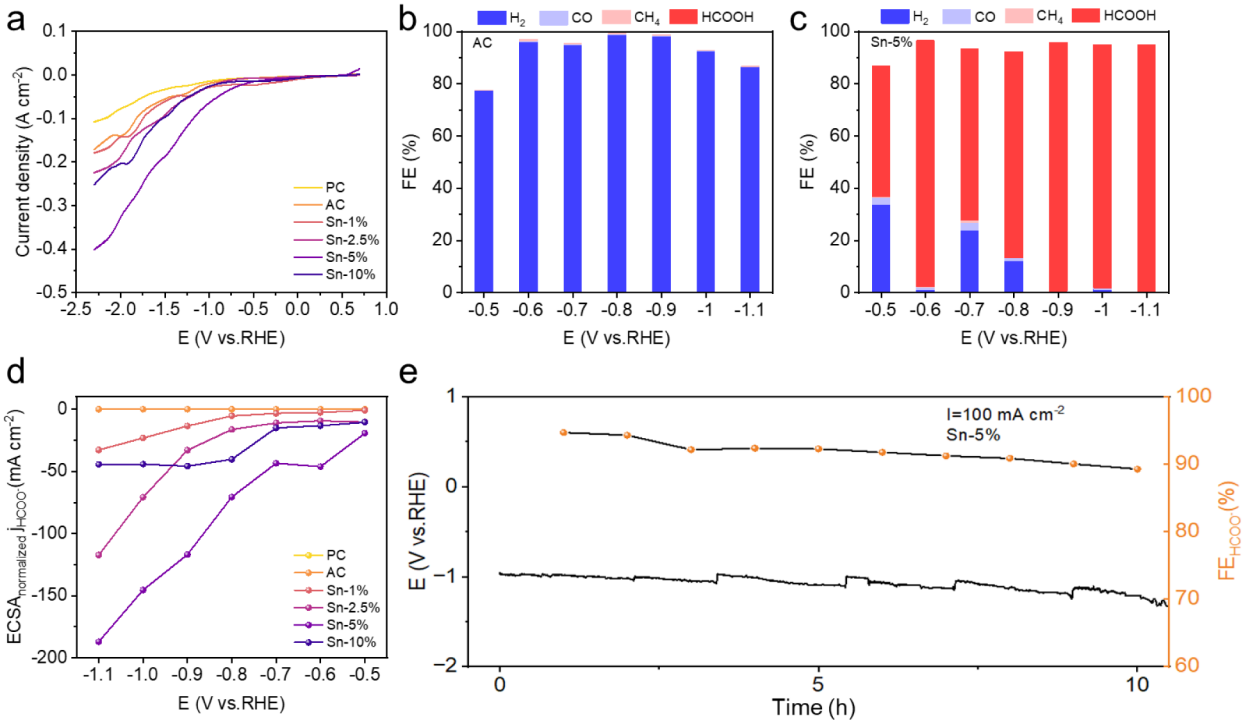

Figure 2. (a) LSV curves of different catalysts in a CO_2 atmosphere. FEs distribution of CO_2RR products on AC (b) and Sn-5% (c) catalysts at different applied potentials. (d) ECSA-normalized $HCOO^-$ partial current densities for different catalysts. (e) Electrochemical stability at −100 mA cm^{-2} under a CO_2 flow rate of 20 sccm for Sn-5%.

TEM images of the synthesized nanocomposites (Figures 1d, e, and S1−S6) were acquired to study the morphology of the materials at the nanoscale. Carbon arranged as thin sheets was exhibited in the TEM images of PC and AC, Figures 1d and S1, respectively. SnO_2 nanoparticles are embedded in the AC matrix, as well as being dispersed on the surface of the AC, as shown in the TEM images of Sn-1%, Sn-2.5%, Sn-5% and Sn-10%. Further, the polydispersity of the nanoparticles increased with increasing Sn loading. Moreover, the number of nanoparticles anchored on the surface rather than being embedded in the matrix increased with increasing Sn loading, as shown in the TEM images. When the Sn loading reaches 5%, it can be observed that a large number of SnO_2 nanoparticles are uniformly dispersed on the material surface. These dispersed sites provide favorable conditions for the formation of $HCOO^-$ (Figure 1e). Nanoparticle aggregation and the production of larger nanoparticles have resulted from increasing the loading of Sn due to the Oswald ripening of the nanoparticles during the hydrothermal treatment, where smaller nanoparticles dissolve into their atoms and redeposit onto larger nanoparticles, decreasing the total number of nanoparticles and increasing the average size, reducing the surface free energy. Small nanorods have been formed in addition to the spherical and irregularly shaped nanoparticles with 10% Sn loading, as shown in Sn-10%. This is due to the growth and Oswald ripening of the nanoparticles in one direction due to the heat and the pressure being applied during the hydrothermal treatment at a high precursor (Sn) concentration (10 wt %). This was quite consistent with the XRD patterns, where no peaks corresponding to SnO_2 were present in Sn loading up to 5%, whereas the peaks attributed to SnO_2 were observed in Sn-10%. However, when the content increases to 10%, significant aggregation of SnO_2 into large particles becomes evident, which is generally considered detrimental to the CO_2RR.

The XRD patterns of the synthesized materials were collected in order to study the crystal nature (Figure 1f). The XRD patterns of the AC and PC show a broad peak around 24°, indicating the presence of amorphous carbon. The XRD patterns of Sn-1%,2.5%, and 5% also show the same broad peak, and no peaks corresponding to any crystal state of Sn_xO_y were observed due to the monodispersity of the nanoparticles on the carbon matrix, and the Sn concentration is insufficient to create a crystalline peak in the XRD pattern.[45] The XRD pattern of the highest Sn-loaded carbon (Sn-10%) shows broad four peaks centered at 26.6°, 33.9°, 38.1°, and 51.8°, indicating the presence of (110), (101), (200), and (211) crystalline peaks of SnO_2 (PDF# 41−1445). The corresponding *d* spacing values are 3.347, 2.642, 2.369, and 1.764 nm, respectively. The crystallite size calculated for the peak with the highest intensity, (110), is 15.98 nm. The nanocomposite is composed of SnO_2 nanoparticles that are distributed on the activated carbon matrix.

The XPS spectra were obtained to study the surface chemistry of the synthesized materials. The survey spectra of the Sn incorporated materials are shown in Figure 1g, and they indicate the presence of C, O, and Sn as the main elements. The higher resolution spectra of Sn in all four Sn-loaded materials were collected (Figure S8). The spin−orbital coupling of the 3d peak splits it to $3d_{5/2}$ and $3d_{3/2}$. The peaks were deconvoluted, and at lower loadings of Sn (<10%), only the +2-oxidation state of Sn was present as revealed by the peaks centered at 486.9 and 495.5 eV, representing $3d_{5/2}$ and $3d_{3/2}$, respectively.[46] The peaks of Sn-10% were deconvoluted into four peaks. The peaks at 486.6 and 494.8 eV correspond to the $3d_{5/2}$ and $3d_{3/2}$ peaks of the +2-oxidation state,[47] whereas the peaks at 487.9 and 496.1 eV are attributed to the

https://doi.org/10.1021/acsenvironau.5c00213
ACS Environ. Au 2026, 6, 144−153

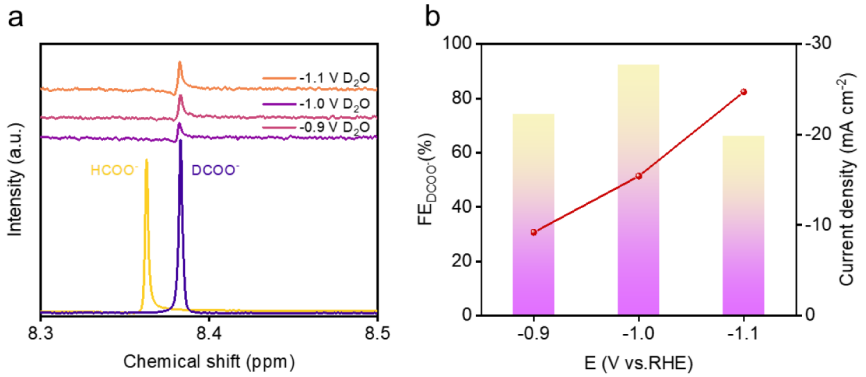

Figure 3. (a) ^{1}H NMR spectrum of D_2O-labeled $HCOO^-$. (b) FE of $DCOO^-$ on Sn-5% in 0.5 M $KHCO_3$ (D_2O).

$3d_{5/2}$ and $3d_{3/2}$ peaks of the +4-oxidation state,[48] revealing the presence of both Sn^{2+} and Sn^{4+} on the nanoparticle surface. Therefore, it is evident that though the crystal consists of SnO_2, the surface bears Sn^{2+}, which are not fully oxidized to form Sn^{4+}.

Raman spectra of the materials were collected to study the crystal nature of the materials, especially focusing on vibrational modes present in carbon-related materials. The Raman spectra are shown in Figure S9. Any Raman band corresponding to oxides of Sn was not present, even in the carbon composite with the highest Sn loading. The peaks related to carbon are only present in all the Raman spectra. The peak around 1340 cm^{-1} corresponds to the D band, which occurs due to the breathing modes of the sp^2 atoms in rings, whereas the peak at 1580 cm^{-1} corresponds to the G band, which represents the bond stretching of all pairs of sp^2 atoms in both rings and chains.[49−51]

Experimental Evaluation of CO_2 Reduction

CO_2RR performance was evaluated in a flow cell using gas diffusion layer (GDL)-loaded Sn catalysts as the cathodes and 0.5 M $KHCO_3$ as the electrolyte. To collect the activity and selectivity of the as-synthesized catalysts, chronoamperometry experiments were conducted over a potential range from −0.5 to −1.1 V vs RHE. The gas-phase products were analyzed using online gas chromatography (GC), and the liquid-phase products were characterized by nuclear magnetic resonance (NMR). The measurable products include H_2, C_1 (CO, CH_4, HCOOH). In this study, the linear sweep voltammetry (LSV) curves over various catalysts were determined (Figure 2a), including PC, AC, Sn-1%, Sn-2.5%, Sn-5% and Sn-10%. It can be observed that the CO_2RR activity of the catalyst is strongly dependent on both the Sn loading content and its chemical state. At the identical applied potential, the Sn-5% catalyst demonstrates the highest current density, indicating superior CO_2RR activity. The $HCOO^-$ partial current density of CO_2RR is catalyzed by different catalysts (Figure S10). With the increase of Sn loading amount, it can be seen that the partial current density for $HCOO^-$ gradually improves within the wide potential range tested. Obviously, the Sn-5% catalyst exhibited significantly higher partial current density for $HCOO^-$ than the other catalysts over the entire wide potential range tested, demonstrating excellent $HCOO^-$ activity. The CO_2RR performance comparison between PC (Figure S11) and AC (Figure 2b) catalysts demonstrates that simple acid-washing activation of coconut shell-derived porous carbon is insufficient to confer CO_2RR activity. Furthermore, at a Sn loading of 5% (Sn-5%), the catalyst exhibited significantly higher $HCOO^-$ selectivity at higher potentials (−0.9 V to −1.1 V) compared to other catalysts (Figure 2c). This indicates that $HCOO^-$ selectivity progressively increases with higher Sn loadings. However, when the loaded Sn exists in the form of SnO_2 clusters (Sn-10%), a significant decrease in $HCOO^-$ selectivity at high potential is observed (−0.9 V to −1.1 V), indicating that the form of Sn is also a key factor affecting the selectivity for $HCOO^-$ (Figure S8). Furthermore, to elucidate the role of the support in enhancing $HCOO^-$ selectivity, SnO_2 was directly synthesized via a hydrothermal method and subjected to CO_2RR testing under identical conditions (Figure S12). The results demonstrate the FE ratio of $HCOO^-$ to CO for SnO_2 is significantly lower than that of Sn-5% (−0.9 V), confirming that dispersing Sn sites on the support facilitates $HCOO^-$ formation.

We further compared the intrinsic activity of the catalysts. The electrochemically active surface area (ECSA) of different catalysts was determined by cyclic voltammetry (Figure S13). It was found that the number of active sites per unit area significantly increased with Sn loading compared (>0.298 mF) to the Sn-free PC (0.117 mF) and AC (0.172 mF) catalysts. This value reached a maximum at a Sn loading of 5 wt % (0.413 mF). However, when the Sn loading was increased to 10 wt % (0.365 mF), where Sn existed predominantly as SnO_2 clusters, the number of active sites decreased markedly, approaching the level observed at the 2.5 wt % Sn loading (0.298 mF) (Figure S14). To better illustrate the differences in intrinsic activity, we normalized the $HCOO^-$ current by the electrochemical surface area (ECSA) (Figure 2d). The results demonstrate that Sn-5% exhibits significantly higher formate partial current densities across the entire tested potential range compared to other catalysts, further confirming its superior selectivity toward $HCOO^-$ formation. This finding aligns well with the previously reported CO_2RR performance results. Moreover, long-term CO_2RR durability was tested under a CO_2 flow rate of 20 sccm. The FE $HCOO^-$ can be maintained above 90% for 10 h at −100 mA cm^{-2} in the 0.5 M $KHCO_3$ electrolyte (Figure 2e). After a 10-h stability test, the overpotential variation remained below 0.3 V (from −0.9 to −1.18 V), indicating no significant degradation. It can be concluded that the catalyst with 5% Sn loading (Sn-5%), where monodispersed SnO_2 is supported on AC, exhibits optimal CO_2RR performance and $HCOO^-$ selectivity.

To elucidate the key steps in CO_2 reduction to $HCOO^-$, we conducted isotope tracing experiments using D_2O as the solvent and verified the liquid products via ^{1}H NMR spectroscopy. The results demonstrate that when H_2O was

https://doi.org/10.1021/acsenvironau.5c00213
ACS Environ. Au 2026, 6, 144−153

replaced by D_2O, the $HCOO^-$ signal in the ^1H NMR spectrum corresponded to the characteristic signal of deuterated formic acid ($DCOO^-$) (Figure 3a). This indicates that under D_2O solvent conditions, the CO_2RR product over Sn-5% is $DCOO^-$, unambiguously proving that the C−H bond in formic acid originates directly from solvent water molecules.

Furthermore, given the lower reactivity of deuterium (D) compared to proton (H), the current density and product selectivity of CO_2RR were notably affected.[32] The greater mass of D compared to H lowers the vibrational frequency of the D−O bond, increasing the energy required for its cleavage. This slows proton-transfer steps during CO_2RR, significantly reducing the current density to approximately 20% of that in H_2O. Nevertheless, the Sn-5% catalyst maintained considerable $DCOO^-$ selectivity (FE > 60%) at high overpotentials, with the FE reaching a maximum of 90% at −1.0 V (Figure 3b). This confirms the superior capability of Sn-5% for deuterated formate production.

Ex-Situ Characterization of Catalysts after CO_2 Reduction

To elucidate the enhanced CO_2RR performance, XPS analysis followed by Sn 3d peak deconvolution was performed on prereaction catalysts with different Sn loadings, with the goal of correlating Sn valence state with $HCOO^-$ selectivity. *Quasi in-situ* XPS analysis of catalysts subjected to 1-h electrolysis at −1.0 V under CO_2RR conditions (Figure 4a) demonstrates

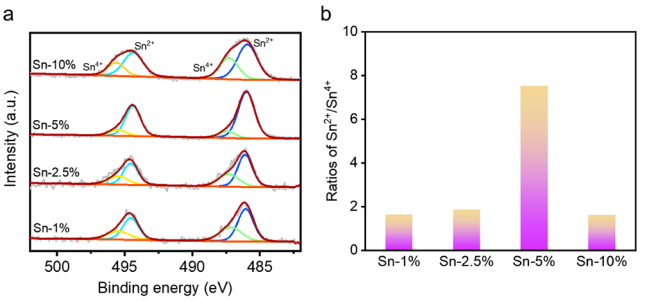

Figure 4. (a) Sn 3d XPS spectrum and (b) the ratios of Sn^{2+}/Sn^{4+} for different Sn-loaded catalysts after CO_2RR.

prominent Sn^{2+} signatures across all postreaction catalysts (486.5 and 494.6 eV) and Sn^{4+} (487.6 eV, 496.1 eV).[52,53] This confirms that SnO_2 loading on AC effectively suppresses the reduction of Sn^{4+} to Sn^0, stabilizing the Sn^{2+} valence state. Notably, the Sn^{2+}/Sn^{4+} ratio reaches 7.52 for Sn-5%, substantially exceeding the 1.60 ratio observed for Sn-10% (Figure 4b). These results indicate that monodisperse SnO_2 loading on porous carbon significantly promotes Sn^{4+}-to-Sn^{2+} conversion during CO_2RR compared to clustered configurations. Crucially, Sn^{2+} is identified as the genuine active site for $HCOO^-$ formation,[28−30] with its content trend aligning with ECSA measurements. This correlation clarifies that the superior $HCOO^-$ productivity of Sn-5% stems from its higher density of active sites.

To investigate the impact of morphology on $HCOO^-$ selectivity, TEM characterization was performed on the catalysts after CO_2RR. According to the TEM images after CO_2RR, the Sn-5% catalyst showed no significant change in the dispersion of Sn sites, while the Sn-10% catalyst still exhibited significant bulk agglomeration (Figure S15). This indicates that the agglomeration induced during the CO_2RR process had a lesser impact on formate selectivity than the inherent agglomeration of the catalyst itself.

Mechanisms of CO_2 Electroreduction to $HCOO^-$ by *In Situ* Spectroscopy

The potential-dependent reduction of the catalysts was monitored using *in situ* Raman and *in-situ* attenuated total reflection Fourier transform infrared spectroscopy (ATR-FTIR) to track their evolution and identify intermediate-catalyst interactions. Building upon prior analysis confirming the superior $HCOO^-$ activity of the Sn-5% catalyst compared to other Sn-loading variants, we further investigated the fundamental origin of its significantly enhanced $HCOO^-$ selectivity through a comparative study of Sn-5% and pristine AC using these dual *in situ* spectroscopic techniques. The applied potential range during *in situ* spectroscopic measurements matched that used in previous CO_2RR experiments (−0.5 V to −1.1 V).

The *in-situ* Raman spectra (Figure 5a−b) revealed a peak at 1580 cm^{-1} for both AC and Sn-5%, assigned to the G-band of

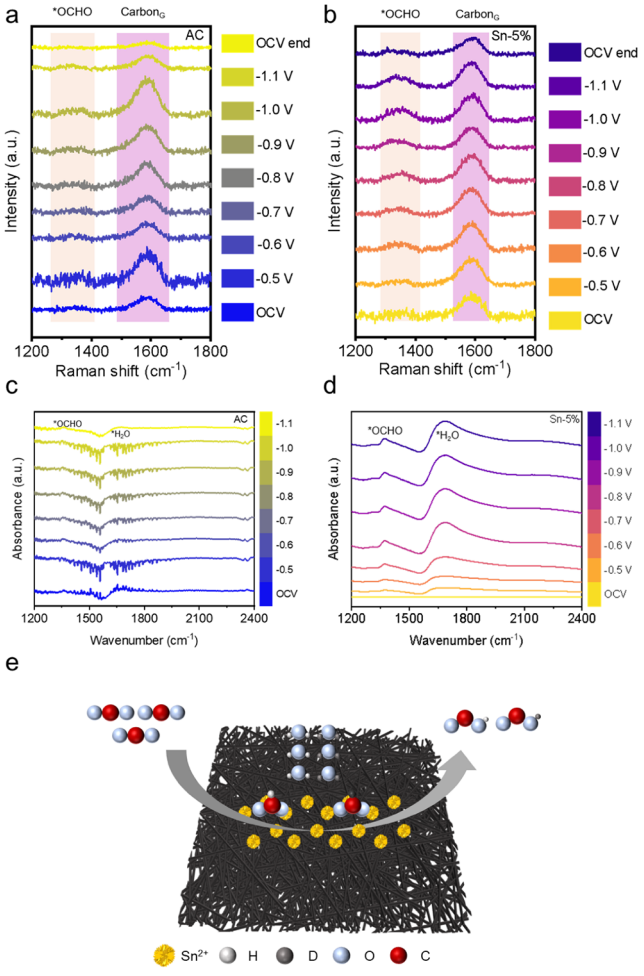

Figure 5. (a−b) *In-situ* electrochemical Raman spectra of the AC (a), Sn-5% (b) catalysts in the CO_2RR at different potentials. (c−d) *In-situ* electrochemical ATR-FTIR spectra of the AC (c), Sn-5% (d) catalysts in the CO_2RR at different potentials. (e) Reaction pathway schematic for the reduction of CO_2 to $HCOO^-$.

carbon (CarbonG).[54] This signal persisted at open circuit voltage (OCV) and after potential removal (OCV end), confirming its irrelevance to the CO_2RR process. A distinct signal in the 1300−1400 cm^{-1} region, attributed to the *OCHO intermediate (a key species for $HCOO^-$ formation)

https://doi.org/10.1021/acsenvironau.5c00213
ACS Environ. Au 2026, 6, 144−153

based on prior literature,[55−57] was notably absent in the AC sample. In contrast, the Sn-5% catalyst exhibited a potential-dependent increase in this *OCHO signal intensity with applied overpotential. These results demonstrate that (i) pristine AC lacks active sites for $HCOO^-$ generation, and (ii) Sn doping facilitates the accumulation of *OCHO intermediates at more negative potentials (−0.5 V to −1.1 V), directly correlating with enhanced $HCOO^-$ production during CO_2RR. This observation aligns with previous electrochemical data, confirming that Sn incorporation significantly improves the FE of AC toward $HCOO^-$ synthesis. No discernible Raman signals were detected in the 200−1200 cm^{-1} or 2200−3000 cm^{-1} regions (Figures S16−S17), further corroborating (i) the low CO_2RR activity of pristine AC and (ii) the high $HCOO^-$ selectivity of Sn-5%, with no detectable reduction products besides $HCOO^-$. This finding is consistent with our experimental product distribution.

Complementary *in-situ* ATR-FTIR spectroscopy was employed to monitor key intermediates during CO_2RR. No characteristic peaks were observed at OCV (Figure 5c−d). Upon applying reduction potentials, two distinct peaks emerged: bands at 1390 cm^{-1} and 1640 cm^{-1}, assigned to the C−O stretching vibration of the *OCHO intermediate and the H−O−H bending vibration of interfacial water molecules, respectively.[58] This confirms CO_2RR proceeds via the *OCHO pathway. Critically, the AC sample exhibited no detectable *OCHO intermediate signals, demonstrating its negligible $HCOO^-$ production capability. Conversely, the *OCHO signal intensity on the Sn-5% catalyst progressively increased with more negative applied potentials, stabilizing beyond −0.8 V. This potential-dependent behavior reflects the activation characteristics of CO_2RR. The trend in *OCHO signal intensity variation with potential aligns well with the measured $HCOO^-$ selectivity,[59,60] highlighting the significant advantage conferred by the 5% monodispersed SnO_2 loading on the AC support.

Based on combined *ex-situ*/*in-situ* characterization, the CO_2-to-$HCOO^-$ pathway can be proposed (Figure 5e). CO_2 undergoes a single-step proton−electron transfer, generating *OCHO (or *OCDO in deuterated experiments) intermediates adsorbed on Sn^{2+} active sites, which subsequently yield $HCOO^-$/$DCOO^-$.

CONCLUSION

In summary, we have successfully achieved the loading of SnO_2 on AC, and the resulting material demonstrates exceptional $HCOO^-$ selectivity in the CO_2RR. Specifically, the FE ($HCOO^-$) achieves 95% with a partial current density of 78.6 $mA{\cdot}cm^{-2}$ in a flow cell. Through comprehensive characterization techniques (including XRD, XPS, *in-situ* Raman spectroscopy, and *in-situ* ATR-FTIR), we reveal that the highly dispersed SnO_2 nanoparticles inhibit the reduction process from Sn^{4+} to Sn^0 during CO_2RR, resulting in the stabilization of Sn species at the +2 oxidation state. The abundant Sn^{2+} species serve as the genuine active sites, facilitating the formation of the *OCHO intermediate and thereby efficiently driving the CO_2 reduction toward $HCOO^-$ production. Additionally, this study achieved the production of $DCOO^-$ by replacing H_2O with D_2O in a flow cell, demonstrating a FE>60% and a current density >10 $mA{\cdot}cm^{-2}$. This work provides valuable insights for the design of high-performance CO_2RR catalysts targeting both $HCOO^-$ and $DCOO^-$ production

Experimental Section

Experimental details on materials and methods are given in the Supplementary Information.

ASSOCIATED CONTENT

Data Availability Statement

The data supporting this article have been included in the main text and Electronic Supporting Information.

Supporting Information

The Supporting Information is available free of charge at https://pubs.acs.org/doi/10.1021/acsenvironau.5c00213.

The detailed preparation methods for porous CH and activated CH, the synthesis procedure for SnO_2 powder, and the deposition protocols for Sn loadings on AC support (Sn-1%, Sn-2.5%, Sn-5%, Sn-10%); characterization descriptions of *in situ* Raman and *in situ* FTIR spectroscopy; SEM and TEM images of PC, AC, Sn-1%, Sn-2.5%, Sn-5%, and Sn-10% (Figures S1−S6); EDS mapping of the Sn-10% sample (Figure S7); high-resolution Sn 3d XPS spectra of catalysts with varying Sn loadings (Figure S8); Raman spectra of different catalysts (Figure S9); $HCOO^-$ partial current densities of the catalysts (Figure S10); CO_2 reduction reaction (CO_2RR) product distributions of PC, Sn-1%, Sn-2.5%, and Sn-10% (Figure S11); comparative CO_2RR product distributions of Sn-5% and SnO_2 at −0.9 V (Figure S12); CV curves at different scan rates and the corresponding calculated ECSA values for various catalysts (Figures S13−S14); post-CO_2RR TEM images of Sn-5% and Sn-10% catalysts (Figure S15); and *in situ* Raman spectra of AC and the Sn-5% catalyst (Figures S16−S17) (PDF)

AUTHOR INFORMATION

Corresponding Authors

Wenlei Zhu − *State Key Laboratory of Water Pollution Control and Green Resource Recycling, State Key Laboratory of Analytical Chemistry for Life Science, Frontiers Science Center for Critical Earth Material Cycling, School of the Environment, School of Chemistry and Chemical Engineering, Nanjing University, Nanjing 210023, China;* orcid.org/0000-0001-6110-993X; Email: wenleizhu@nju.edu.cn

Yang Zhou − *State Key Laboratory of Flexible Electronics & Institute of Advanced Materials (IAM), Nanjing University of Posts & Telecommunications, Nanjing 210023, China;* Email: iamyangzhou@njupt.edu.cn

Charitha Thambiliyagodage − *Department of Applied Sciences, Faculty of Humanities and Sciences, Sri Lanka Institute of Information Technology, Malabe 10115, Sri Lanka;* orcid.org/0000-0003-0906-4441; Email: charitha.t@sliit.lk

Authors

Chen Qin − *State Key Laboratory of Water Pollution Control and Green Resource Recycling, State Key Laboratory of Analytical Chemistry for Life Science, Frontiers Science Center for Critical Earth Material Cycling, School of the Environment, School of Chemistry and Chemical Engineering, Nanjing University, Nanjing 210023, China*

https://doi.org/10.1021/acsenvironau.5c00213
ACS Environ. Au 2026, 6, 144−153

Gevindu Masakorala − *Department of Applied Sciences, Faculty of Humanities and Sciences, Sri Lanka Institute of Information Technology, Malabe 10115, Sri Lanka*
Muhammed Mohideen − *Department of Applied Sciences, Faculty of Humanities and Sciences, Sri Lanka Institute of Information Technology, Malabe 10115, Sri Lanka*
Thisus Samarasekara − *Department of Applied Sciences, Faculty of Humanities and Sciences, Sri Lanka Institute of Information Technology, Malabe 10115, Sri Lanka*
Long Zhang − *State Key Laboratory of Flexible Electronics & Institute of Advanced Materials (IAM), Nanjing University of Posts & Telecommunications, Nanjing 210023, China*

Complete contact information is available at: https://pubs.acs.org/10.1021/acsenvironau.5c00213

Author Contributions

W.Z. conceived the idea. W.Z., Y.Z. and C.T. supervised the project. G.M., M.M., L.Z. and T.S. synthesized catalysts. C.Q. tested catalytic performance and conducted catalyst characterization. C.Q., W.Z. and C.T. analyzed the data and wrote the paper. All authors discussed the results and commented on the paper. CRediT: **Chen Qin** conceptualization, data curation, writing - original draft; **Gevindu Masakorala** conceptualization; **Muhammed Mohideen** conceptualization; **Thisus Samarasekara** conceptualization; **Long Zhang** resources; **Yang Zhou** supervision; **Charitha Thambiliyagodage** supervision.

Notes

The authors declare no competing financial interest.

■ ACKNOWLEDGMENTS

W. Z. would like to acknowledge the support from State Key Laboratory of Analytical Chemistry for Life Science (SKLACLS2503), National Natural Science Foundation of China (22176086), the Fundamental Research Funds for the Central Universities (021114380222, 021114380214), and the Research Funds from Frontiers Science Center for Critical Earth Material Cycling of Nanjing University. Charitha Thambiliyagodage would like thank the research grant awarded by Sri Lanka Institute of Information Technology Research Grant Number: PVC(R&I)/RG/2025/2.

■ REFERENCES

(1) Fu, J.; Li, P.; Lin, Y.; Du, H.; Liu, H.; Zhu, W.; Ren, H. Fight for carbon neutrality with state-of-the-art negative carbon emission technologies. *Eco-Environ. Health* **2022**, *1*, 259−279.
(2) Wang, X.; Hu, Y.; Zhou, Y.; Zhu, S.; Cui, J.; Song, B.; Zhu, W. High-performance electrocatalytic reduction of carbon dioxide to carbon monoxide using biochar-supported gold nanoparticles. *Energy Fuels* **2025**, *39*, 9907−9916.
(3) Hu, Y.; Wang, X.; Liu, J.; Lu, X.; Huang, L.; Jiang, Y.; Zhao, L.; Li, J.; Yin, Z.; Cui, J.; et al. Constructing fecal-derived electrocatalysts for CO_2 upcycling: simultaneously tackling waste and carbon emissions. *Nanoscale* **2025**, *17*, 5056−5063.
(4) Zhuang, Z.; Wang, G.; Zhao, W.; Yang, R.; Zhou, Y.; Zhu, W. Silver-doped porous copper catalysts for efficient resource utilization of CO-containing flue gases. *ACS Environ. Au* **2025**, *5*, 287−297.
(5) Luo, H.; Lu, X.; Cao, Y.; Lyu, Z.; Ding, S.; Lin, Y.; Zhou, Y.; Zhu, W.; Wang, Y. Boosted CO_2 photoreduction performance by CdSe nanoplatelets via Se vacancy engineering. *Adv. Sci.* **2025**, *12*, No. e2413684.
(6) Liu, Z.; Xu, B.; Jiang, Y.-J.; Zhou, Y.; Sun, X.; Wang, Y.; Zhu, W. Photocatalytic conversion of methane: Current state of the art, challenges, and future perspectives. *ACS Environ. Au* **2023**, *3*, 252−276.
(7) Cai, Y.; Yang, R.; Fu, J.; Li, Z.; Xie, L.; Li, K.; Chang, Y.-C.; Ding, S.; Lyu, Z.; Zhang, J.-R.; Zhu, J.-J.; Lin, Y.; Zhu, W. Self-pressurizing nanoscale capsule catalysts for CO_2 electroreduction to acetate or propanol. *Nat. Synth.* **2024**, *3* (7), 891−902.
(8) Ma, Q.; Cheng, J.; Wu, X.; Xie, J.; Zhang, R.; Mao, Z.; Yang, H.; Fan, W.; Zeng, J.; Bitter, J. H.; et al. C−C bond coupling with sp^3 C−H bond via active intermediates from CO_2 hydrogenation. *Nat. Commun.* **2025**, *16* (1), 140.
(9) Zhong, M.; Tran, K.; Min, Y.; Wang, C.; Wang, Z.; Dinh, C.-T.; De Luna, P.; Yu, Z.; Rasouli, A. S.; Brodersen, P.; Sun, S.; Voznyy, O.; Tan, C.-S.; Askerka, M.; Che, F.; Liu, M.; Seifitokaldani, A.; Pang, Y.; Lo, S.-C.; Ip, A.; Ulissi, Z.; Sargent, E. H. Accelerated discovery of CO_2 electrocatalysts using active machine learning. *Nature* **2020**, *581* (7807), 178−183.
(10) Hepburn, C.; Adlen, E.; Beddington, J.; Carter, E. A.; Fuss, S.; Mac Dowell, N.; Minx, J. C.; Smith, P.; Williams, C. K. The technological and economic prospects for CO_2 utilization and removal. *Nature* **2019**, *575* (7781), 87−97.
(11) Kim, I.; Lee, G.-B.; Kim, S.; Jung, H. D.; Kim, J.-Y.; Lee, T.; Choi, H.; Jo, J.; Kang, G.; Oh, S.-H.; Kwon, W.; Hong, D.; Kim, H. G.; Lee, Y.; Kim, U.; Kim, H.; Kim, M.; Back, S.; Park, J.; Joo, Y.-C.; Nam, D.-H. Unveiling the reconstruction of copper bimetallic catalysts during CO_2 electroreduction. *Nat. Catal.* **2025**, *8* (7), 697−713.
(12) Ou, Y.; Liu, L.; Seemakurthi, R. R.; You, F.; Ma, H.; Pérez-Ramírez, J.; López, N.; Yeo, B. S. Controlling hydrocarbon chain growth and degree of branching in CO_2 electroreduction on fluorine-doped nickel catalysts. *Nat. Catal.* **2025**, *8* (7), 714−727.
(13) Liu, J.; Guo, X.; Lyu, Z.; Song, R.-B.; Zhou, P.; Ding, S.; Zhou, Y.; Jiang, L.-P.; Lin, Y.; Zhu, W. A novel tandem reactor design based on nano-Cu electrocatalysts and microbial biocatalysts for converting CO_2 into ethylene and acetate. *Green Chem.* **2023**, *25* (14), 5712−5720.
(14) Jiang, Y.; Tian, S.; Li, H.; Xia, A.; Song, B.; Zhu, W. Harnessing microbial electrosynthesis for a sustainable future. *Innov. Mater* **2023**, *1*, 100008.
(15) Deng, Y.; Zhao, J.; Wang, S.; Chen, R.; Ding, J.; Tsai, H.-J.; Zeng, W.-J.; Hung, S.-F.; Xu, W.; Wang, J.; Jaouen, F.; Li, X.; Huang, Y.; Liu, B. Operando Spectroscopic Analysis of Axial Oxygen-Coordinated Single-Sn-Atom Sites for Electrochemical CO_2 Reduction. *J. Am. Chem. Soc.* **2023**, *145* (13), 7242−7251.
(16) Ye, N.; Wang, K.; Tan, Y.; Qian, Z.; Guo, H.; Shang, C.; Lin, Z.; Huang, Q.; Liu, Y.; Li, L.; Gu, Y.; Han, Y.; Zhou, C.; Luo, M.; Guo, S. Industrial-level CO_2 to Formate Conversion on Turing-Structured Electrocatalysts. *Nat. Synth* **2025**, *4* (7), 799−807.
(17) Yang, S.; An, H.; Arnouts, S.; Wang, H.; Yu, X.; de Ruiter, J.; Bals, S.; Altantzis, T.; Weckhuysen, B. M.; van der Stam, W. Halide-Guided Active Site Exposure in Bismuth Electrocatalysts for Selective CO_2 Conversion into Formic Acid. *Nat. Catal.* **2023**, *6* (9), 796−806.
(18) Klinkova, A.; De Luna, P.; Dinh, C.-T.; Voznyy, O.; Larin, E. M.; Kumacheva, E.; Sargent, E. H. Rational Design of Efficient Palladium Catalysts for Electroreduction of Carbon Dioxide to Formate. *ACS Catal.* **2016**, *6* (12), 8115−8120.
(19) Rahaman, M.; Dutta, A.; Broekmann, P. Size-Dependent Activity of Palladium Nanoparticles: Efficient Conversion of CO_2 into Formate at Low Overpotentials. *ChemSusChem* **2017**, *10* (8), 1733−1741.
(20) Min, X.; Kanan, M. W. Pd-Catalyzed Electrohydrogenation of Carbon Dioxide to Formate: High Mass Activity at Low Overpotential and Identification of the Deactivation Pathway. *J. Am. Chem. Soc.* **2015**, *137* (14), 4701−4708.
(21) Yan, J.; Jiang, C.; Zeng, X.; Song, W.; Yang, J.; Ge, X.; Wu, L.; Yang, Z.; Li, Z.; Wang, Y.; Xu, T. Synthesis of deuterated acids and bases using bipolar membranes. *Nature* **2025**, *643* (8073), 961−966.
(22) Li, X.; Qin, C.; Wang, C.; Pan, F.; Chen, K.-J. In situ formed CuSn alloy from multivariate metal−organic frameworks for tunable CO_2 electroreduction. *Chem. Commun.* **2025**, *61* (12), 2544−2547.

(23) Wu, S.; Li, S.; Hou, Z.; Hu, Y.; Zhang, Z.; Zhu, J.; Xu, S.; Wang, R.; Zhang, N.; An, L.; et al. Dual-Site Activation for Efficient Acidic CO_2 Electroreduction at Industrial-Level Current Densities. *Adv. Mater.* **2025**, *37* (37), 2503772.
(24) Zhang, W.; Mao, Q.; Ding, J.; Liu, Q.; Wang, S.; Wang, J.; Li, X.; Yang, H.; Liu, B. S-doped Ag-Sn Alloy Hollow Microbox for High-Performance CO_2 Electroreduction to Formate. *Angew. Chem. Int. Ed.* **2025**, *64*, No. e202510743.
(25) Wei, Y.; Wang, X.; Mao, J.; Song, Y.; Zhu, H.; Liu, X.; Luo, C.; Li, S.; Chen, A.; Li, G.; et al. Chlorine-Doped SnO_2 Nanoflowers on Nickel Hollow Fiber for Enhanced CO_2 Electroreduction at Ampere-Level Current Densities. *Angew. Chem. Int. Ed.* **2025**, *64* (13), No. e202423370.
(26) Li, B.; Chen, J.; Wang, L.; Xia, D.; Mao, S.; Xi, L.; Ying, S.; Zhang, H.; Wang, Y. Dynamic Reconstruction of Cu-Doped SnO_2 for Efficient Electrochemical Reduction of CO_2 to Formate. *Appl. Catal. B: Environ.* **2025**, *363*, 124784.
(27) Jiang, Y.; Shan, J.; Wang, P.; Huang, L.; Zheng, Y.; Qiao, S.-Z. Stabilizing Oxidation State of SnO_2 for Highly Selective CO_2 Electroreduction to Formate at Large Current Densities. *ACS Catal.* **2023**, *13* (5), 3101−3108.
(28) Puppin, L. G.; da Silva, L. F.; Carmo, M.; Varela, H.; Lopes, O. F. Effect of the oxidation state and morphology of SnO_x-based electrocatalysts on the CO_2 reduction reaction. *J. Mater. Res.* **2021**, *36* (20), 4240−4248.
(29) Baruch, M. F.; Pander, J. E.; White, J. L.; Bocarsly, A. B. Mechanistic Insights into the Reduction of CO_2 on Tin Electrodes using in Situ ATR-IR Spectroscopy. *ACS Catal.* **2015**, *5* (5), 3148−3156.
(30) Fan, L.; Xia, Z.; Xu, M.; Lu, Y.; Li, Z. 1D SnO_2 with Wire-in-Tube Architectures for Highly Selective Electrochemical Reduction of CO_2 to C_1 Products. *Adv. Funct. Mater.* **2018**, *28* (17), 1706289.
(31) Heng, J.-M.; Zhu, H.-L.; Zhao, Z.-H.; Liao, P.-Q.; Chen, X.-M. Fabrication of Ultrahigh-Loading Dual Copper Sites in Nitrogen-Doped Porous Carbons Boosting Electroreduction of CO_2 to C_2H_4 Under Neutral Conditions. *Adv. Mater.* **2025**, *37* (4), 2415101.
(32) Wang, M.; Liu, S.; Liu, Y.; Zhou, L.; Fan, Y.; Guo, W.; Zhao, Y.; Zheng, G.; Hou, Y. Thermodynamic Miscibility-Guided Engineering of Bismuth−Tin Janus Catalysts for Durable Electrocatalytic CO_2 Reduction. *Angew. Chem. Int. Ed.* **2025**, *64*, No. e202512349.
(33) You, X.; Yang, C.; Li, X.; Tang, Z. Porousizing catalysts for boosting CO_2 electroreducation. *Chin. J. Catal.* **2024**, *67*, 4−20.
(34) Tao, H.; Wang, S.; Liu, H.; Lian, C. Deep Neural Network Enhanced Mesoscopic Thermodynamic Model for Unlocking the Electrode/Electrolyte Interface. *Angew. Chem., Int. Ed.* **2025**, *64* (6), No. e202418447.
(35) Huang, P.; Leng, Y.; Lian, C.; Liu, H. Porous-DeepONet: Learning the solution operators of parametric reactive transport equations in porous media. *Engineering* **2024**, *39* (8), 94−103.
(36) Bai, J.; Huang, J.; Yu, Q.; Demir, M.; Akgul, E.; Altay, B. N.; Hu, X.; Wang, L. Fabrication of Coconut Shell-Derived Porous Carbons for CO_2 Adsorption Application. *Front. Chem. Sci. Eng.* **2023**, *17* (8), 1122−1130.
(37) Tan, Y. C.; Jia, S.; Tan, J.; Leow, Y.; Zheng, R.; Tan, X. Y.; Dolmanan, S. B.; Zhang, M.; Yew, P. Y. M.; Ni, X. P.; et al. Coconut Husk-Derived Biochar for Enhancing Electrochemical Conversion of CO_2. *Mater. Today Chem.* **2023**, *30*, 101595.
(38) Lin, Y.; Lian, C.; Berrueta, M. U.; Liu, H.; van Roij, R. Microscopic Model for Cyclic Voltammetry of Porous Electrodes. *Phys. Rev. Lett.* **2022**, *128* (20), 206001.
(39) Lian, C.; Janssen, M.; Liu, H.; van Roij, R. Blessing and Curse: How a Supercapacitor's Large Capacitance Causes its Slow Charging. *Phys. Rev. Lett.* **2020**, *124* (7), 076001.
(40) Ke, T.; Yun, S.; Wang, K.; Xing, T.; Dang, J.; Zhang, Y.; Sun, M.; An, J.; Liu, L.; Liu, J. Constructing bimetal, alloy, and compound-modified nitrogen-doped biomass-derived carbon from coconut shell as accelerants for boosting methane production in bioenergy system. *Energy Mater.* **2024**, *4* (1), 400011.
(41) Khajuria, A.; Kaushal, J.; Sudan, S. Encapsulated cobalt-doped coconut husk biochar (Co@CHBc) for the remediation of anionic dye from wastewater. *Biomass. Convers. Biorefin* **2025**, *15* (4), 6037−6054.
(42) Singh, P.; Dubey, P.; Younis, K.; Yousuf, O. A review on the valorization of coconut shell waste. *Biomass. Convers. Biorefin* **2024**, *14* (7), 8115−8125.
(43) Ye, Z.; Shen, B.; Kang, D.; Shen, J.; Huang, J.; Wang, Z.; Huang, L.; Wolverton, C. M.; Mirkin, C. A. A data-driven approach for the guided regulation of exposed facets in nanoparticles. *Nat. Synth.* **2024**, *3* (7), 922−929.
(44) Liu, J.; Burciaga, R.; Tang, S.; Ding, S.; Ran, H.; Zhao, W.; Wang, G.; Zhuang, Z.; Xie, L.; Lyu, Z.; Lin, Y.; Du, A.; Yuan, A.; Fu, J.; Song, B.; Zhu, J.; Sun, Z.; Jin, X.; Huo, Z.-Y.; Shen, B.; Shen, M.; Cao, Y.; Zhou, Y.; Jiang, Y.; Zhu, D.; Sun, M.; Wu, X.; Qin, C.; Jiang, Z.; Metin, O.; Thambiliyagodage, C. J.; Lv, J.-J.; Li, Q.; Wu, H.; Wu, Z.; Lam, J. C.-H.; Gao, G.; Li, C.; Luo, M.; Jiang, Y.; Wang, X.; Li, J.; Liu, M.; Lin, R.; Ren, H.; Han, B.; Jing, Y.; Zhu, W. Heterogeneous catalysis for the environment. *Innov. Mater.* **2024**, *2* (3), 100090.
(45) Zhou, L.; Qu, Z.; Fu, L.; Ding, Y. Interfacial Engineering of In-SnO_2 Heterostructure for Promoting Electrocatalytic CO_2 Reduction to Formate. *Appl. Catal. B: Environ.* **2025**, *377*, 125471.
(46) Li, H.; Hai, G.; Wang, Z.; Chen, X.; Bai, S.; Zhang, N.; Liu, T. In situ construction of a crystalline/amorphous interface in SnO_2/Bi nanobelts for efficient CO_2 electroreduction. *J. Mater. Chem. A* **2025**, *13* (20), 14786−14795.
(47) Zhang, M.; Zhang, Z.; Zhao, Z.; Huang, H.; Anjum, D. H.; Wang, D.; He, J.-H.; Huang, K.-W. Tunable Selectivity for Electrochemical CO_2 Reduction by Bimetallic Cu−Sn Catalysts: Elucidating the Roles of Cu and Sn. *ACS Catal.* **2021**, *11* (17), 11103−11108.
(48) Li, Q.; Fu, J.; Zhu, W.; Chen, Z.; Shen, B.; Wu, L.; Xi, Z.; Wang, T.; Lu, G.; Zhu, J.-J.; Sun, S. Tuning Sn-Catalysis for Electrochemical Reduction of CO_2 to CO via the Core/Shell Cu/SnO_2 Structure. *J. Am. Chem. Soc.* **2017**, *139* (12), 4290−4293.
(49) Liu, C.; Zhang, H.; Zhou, W.; Tian, X.; Zhang, T.; Niu, S.; Li, J.; Cao, M.; Wang, Q.; Lv, F.; et al. Air-stable Li_5FeO_4 additive enabled by carbon coating for energy-dense lithium-ion batteries. *Nat. Commun.* **2025**, *16* (1), 7694.
(50) Lei, J.; Li, S.; Shen, Y.; Wang, X.; Yang, X.; Wu, H.; Guo, H.; Liu, H.; Zhang, D.; Wang, S. Ultrafast Synthesis of MOF-Derived Magnetic Ni@C Catalyst for Efficient Photo-Enhanced Uranium Recovery in Real Nuclear Wastewater. *ACS Nano* **2025**, *19*, 31818−31828.
(51) Cai, Q.; Meng, Y.; Wu, C.; Qu, W.; Wang, Q.; Li, T.; Liu, C.; Chen, J.; Lin, H.; He, Q.; et al. De-Saturation of Single-Atom Copper Catalysts for Accelerating Propargylic Substitution Reactions. *Adv. Mater.* **2025**, No. e09221.
(52) Yue, C.; Yang, X.; Zhang, X.; Wang, S.; Xu, W.; Chen, R.; Wang, J.; Yin, J.; Huang, Y.; Li, X. Secondary Coordination Sphere Engineering of Single-Sn-Atom catalyst via P Doping for Efficient CO_2 Electroreduction. *Adv. Energy Mater.* **2024**, *14* (38), 2401448.
(53) Zhang, Y.; Cao, K.; Yang, M.; Hong, H.; Shen, Y.; Ning, H.; Xia, J.; Chen, S. In Situ Polymerization Strategy for Improving the Stability of Sn-Based Perovskite Solar Cells. *ACS Appl. Mater. Interfaces* **2024**, *16* (25), 32240−32248.
(54) Kalbac, M.; Farhat, H.; Kong, J.; Janda, P.; Kavan, L.; Dresselhaus, M. S. Raman Spectroscopy and in Situ Raman Spectroelectrochemistry of Bilayer $^{12}C/^{13}C$ Graphene. *Nano Lett.* **2011**, *11* (5), 1957−1963.
(55) Yang, Y.; Zhou, J.; Zhou, L.; Li, H.; Xie, R.; Zeng, X.; Liu, Y.; Zhi, Y.; Shan, S.; Yao, K. Pulsed Electrocatalysis on SnO_2 Electrodes for Boosting Formate Selectivity and Activity during CO_2 Electro-reduction. *Adv. Funct. Mater.* **2025**, *35*, 2425346.
(56) Chen, X.; Chen, J.; Chen, H.; Zhang, Q.; Li, J.; Cui, J.; Sun, Y.; Wang, D.; Ye, J.; Liu, L. Promoting Water Dissociation for Efficient Solar Driven CO_2 Electroreduction via Improving Hydroxyl Adsorption. *Nat. Commun.* **2023**, *14* (1), 751.

https://doi.org/10.1021/acsenvironau.5c00213
ACS Environ. Au 2026, 6, 144−153

(57) Vasileff, A.; Zhi, X.; Xu, C.; Ge, L.; Jiao, Y.; Zheng, Y.; Qiao, S.-Z. Selectivity Control for Electrochemical CO_2 Reduction by Charge Redistribution on the Surface of Copper Alloys. *ACS Catal.* **2019**, *9* (10), 9411−9417.
(58) Liu, Z.; Liu, C.; Zhang, J.; Mao, S.; Liang, X.; Hu, H.; Huang, X. Efficient and Stable CO_2 to Formate Conversion Enabled by Edge-Site-Enriched SnS_2 Nanoplates. *Appl. Catal. B: Environ.* **2024**, *341*, 123274.
(59) Sun, B.; Li, Z.; Xiao, D.; Liu, H.; Song, K.; Wang, Z.; Liu, Y.; Zheng, Z.; Wang, P.; Dai, Y.; et al. Unveiling pH-Dependent Adsorption Strength of $*CO_2^-$ Intermediate over High-Density Sn Single Atom Catalyst for Acidic CO_2-to-HCOOH Electroreduction. *Angew. Chem. Int. Ed.* **2024**, *63* (14), No. e202318874.
(60) Fan, T.; Zhang, J.; Zhang, X.; Wang, M.; Yi, X.; Lum, Y.; Chen, Z. Interface-Stabilized High-Valent Sn Enables Efficient CO_2 Electroreduction to Formate/Formic Acid across the Full pH Range. *Nano Energy* **2024**, *130*, 110135.

https://doi.org/10.1021/acsenvironau.5c00213
ACS Environ. Au 2026, 6, 144−153